# Wide-Frequency Power Decoupling and Accurate Reactive Power Control for Andronov–Hopf Virtual Oscillator-Based Grid-Forming Inverters

Mingyue Wang, Alian Chen, *Member, IEEE*, Yaopeng Huang, Xianzhe Pang, *Student Member, IEEE*, Cheng Cheng, *Member, IEEE*, and Tong Liu, *Member, IEEE*

***Abstract*—The Andronov–Hopf virtual oscillator control is a grid-forming control strategy based on instantaneous current feedback, which provides voltage and frequency support in weak grids. However, the unavoidable power coupling and inherent inaccuracies in power tracking control lead to steady-state errors and dynamic oscillations, which severely restrict the power delivery and the grid support capability. Therefore, this article proposes an optimized loop-shaping-based power control (OLPC) strategy to ensure system stability. First, to address the inability of the relative gain array to evaluate feedback dynamics, a closed-loop transfer function array is developed. It explicitly reveals two limitations: failure to achieve power decoupling and amplification of reactive power tracking errors. Subsequently, the objectives of OLPC are formulated in the frequency domain using bandwidth design specifications. Then, the optimal parameters are obtained by reformulating the parameter design problem as a convex optimization problem. Compared to the virtual inductor methods, the OLPC exhibits superior wide-frequency power decoupling, more accurate reactive power tracking, and faster power response. Finally, the theoretical analysis and proposed method are validated through experiments.**

***Index Terms*—Accurate reactive power control, grid-forming inverters, loop shaping, virtual oscillator control, wide-frequency power decoupling.**

## I. Introduction

NOWADAYS, inverter-based renewable-energy distributed generation (DG) has attracted significant attention owing to its environmentally friendly energy solutions. With the widespread of DGs, the line impedance increases significantly, leading to large voltage fluctuations at the point of common coupling (PCC), which characterizes weak grids [1]. As a current source, conventional grid-following (GFL) inverters employ a phase-locked loop to synchronize with the grid voltage phase. Under weak grids, the GFL exhibits an inherent inability to provide voltage support, which increases the risk of instability in the power system.

In contrast to GFL, the grid-forming control (GFM) simulates the operation characteristic of synchronous generations (SGs), which provides voltage and frequency support to accommodate weak grids [2]. Motivated by the quasi-steady-state operation of SGs, several GFM control strategies have been proposed, including droop control [3], virtual synchronous generator (VSG) [4], matching control [5], and virtual oscillator control (VOC) [6]. Among GFM strategies, VOCs exhibit faster transient response dynamics, inherently self-sustained periodic voltage generation, and communication-free self-synchronization capabilities for islanded inverters. Thus, VOCs have attracted more attention, particularly the Andronov-Hopf virtual oscillator control (AH-VOC), which stands out for harmonic-free voltage output and enhanced dispatchability in grid-connected mode [7]. However, the interplay between power coupling and reactive power tracking errors exacerbates reactive power deviations and induces oscillations, degrading the voltage support capability. In severe conditions, this may compromise the stable operation of the system [8].

The AH-VOC based inverters independently regulate active power via the power angle and reactive power through output voltage. However, in low-voltage systems with a high line impedance ratio $R/X$, the coupling between the active and reactive power loops becomes significantly strong. Wide-frequency power coupling comprises both steady-state and dynamic components. Steady-state power coupling causes the inverters to absorb excessive reactive from the grid, which restricts active power delivery capability and may threaten the stable operation [9]. Dynamic power coupling may propagate power oscillations between the active power loop and reactive power loop, which degrades the dynamic response performance and potentially induces system instability [10].

To mitigate the power coupling issues, scholars have developed many strategies broadly classified into three categories: 1) the virtual power methods [11], [12], [13], [14]; 2) feedback compensation methods [15], [16], [17], [18]; and 3) virtual

Received 11 April 2025; revised 17 July 2025; accepted 18 September 2025. Date of publication 6 October 2025; date of current version 19 January 2026. This work was supported in part by the National Key Research and Development Program of China under Grant 2022YFB2402900, in part by Shandong Provincial Major Scientific and Technological Innovation Project under Grant 2024CXGC010307, and in part by the China Postdoctoral Science Foundation under Grant 2024M751807. Recommended for publication by Associate Editor T. Jimichi. *(Corresponding author: Alian Chen.)*

Mingyue Wang, Alian Chen, Yaopeng Huang, Xianzhe Pang, and Cheng Cheng are with the School of Control Science and Engineering, Shandong University, Jinan 250061, China (e-mail: mingyuewang@mail.sdu.edu.cn; chenalian@sdu.edu.cn).

Tong Liu is with the School of Future Technology, Shandong University, Jinan 250061, China (e-mail: tong@sdu.edu.cn).

Color versions of one or more figures in this article are available at https://doi.org/10.1109/TPEL.2025.3618108.

Digital Object Identifier 10.1109/TPEL.2025.3618108

impedance methods [19], [20], [21], [22], [23],[24]. In terms of steady-state power decoupling, two factors $R/X$ and power angle were analyzed in [17]. Both the virtual power method [11] and the virtual voltage-frequency method [12] employed a linear coordinate transformation related to the line impedance angle. Nevertheless, these methods focus exclusively on $R/X$ and the power coupling still exists. In [15], a voltage at the point of common coupling estimator (VPCCE) method was proposed to address the effects of $R/X$ ratio and power angle. However, this method cannot adapt to operating point changes. In [19], a virtual inductor was proposed to decrease $R/X$. Whereas, this method inevitably induces a voltage drop that restricts decoupling performance [21]. A q-axis voltage-drop-based power decoupling control (QVPDC) was proposed in [22], which enhances voltage compensation by eliminating the $d$-axis voltage drop. However, this method struggles to adapt to operating point variations and exhibits poor dynamic decoupling performance.

In terms of dynamic power decoupling, a unified transfer function-based analysis tool was employed to investigate the impact of VSG parameters on dynamic power coupling [25]. In [18], a feedback compensation matrix was introduced to mitigate dynamic power coupling. However, it only considers $R/X$ and the steady-state error still exists. In [23], a simplified internal model method was proposed to address power dynamic coupling issues in strong grids and effectively suppress low-frequency oscillations. Whereas its assumptions do not hold in the weak grid. The virtual inductor and virtual capacitor method effectively broadened the selection range for virtual inductance and successfully mitigated reactive power fluctuations [24]. Nevertheless, this method relies on estimating the line impedance and its analysis of wide-frequency power decoupling remains insufficient. Therefore, the above power decoupling methods exhibit limited adaptability to operating point variations and inadequate analysis of wide-frequency power decoupling, compromising power delivery and system stability.

On the other hand, the influence of power decoupling methods on reactive power tracking remains unclear. Despite achieving decoupled power control, inaccuracies in reactive power tracking still are a serious issue, which parallels challenges in GFMs. In [26], a drooped voltage reference adjustment strategy was implemented to enhance the power tracking performance. An embedding secondary control into the droop control was proposed to resolve the mismatches between droop control and line impedance [27]. Similarly, the limitations of AH-VOC in active and reactive power tracking were explained mathematically in [28]. An improved adaptive power tracking method was proposed [29]. However, it has a high sensitivity to the estimation of line impedance and does not take into account dynamic tracking characteristics. Thus, achieving accurate and rapid reactive power control remains challenging, which limits system stability.

To ensure the stable operation of the system, this article proposes an optimized loop-shaping-based power control (OLPC) strategy to achieve wide-frequency power decoupling and accurate reactive power control. The main contributions are summarized as follows.

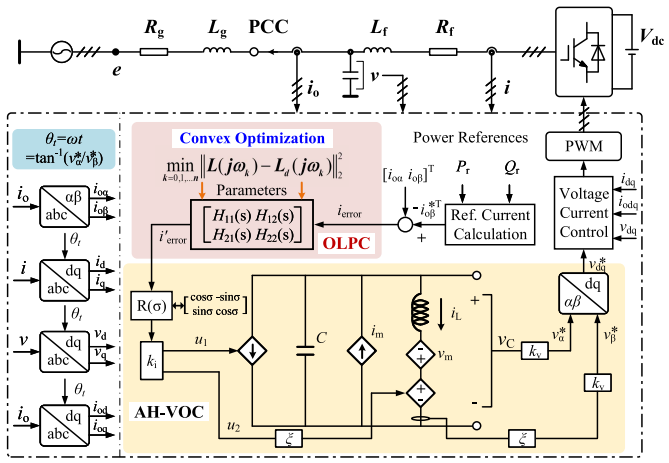


Fig. 1. Circuit and block diagram of the AH-VOC-based inverter with proposed OLPC strategy.

1) This article first examines the limitation of the relative gain array (RGA) in evaluating feedback dynamics and develops a closed-loop transfer function array (CTFA) for power control and robustness analysis. The CTFA reveals the limitations in wide-frequency power decoupling and the tendency to exacerbate inaccuracies in reactive power tracking. This method is applicable to other decoupling methods, such as the virtual inductor method and the QVPDC method.
2) The OLPC strategy is proposed to mitigate both steady-state and dynamic power coupling caused by high $R/X$ and large power angles. The OLPC strategy demonstrates adaptability to variations in amplitude and frequency of active power reference.
3) The dual requirements of accurate reactive power tracking and wide-frequency power decoupling are formulated as a frequency-domain transfer function design problem, with optimal parameters derived through convex optimization techniques.

The rest of this article is organized as follows. Section II establishes the small-signal model of the AH-VOC-based inverters, including the AH-VOC dynamics and plant model. Section III develops the CTFA to analyze the limitations of virtual inductor methods in wide-frequency power decoupling and reactive power control. And the detailed design procedure and principle of OLPC strategy are proposed. Section IV theoretically validates its advantages and robustness using RGA and CTFA methods. Experimental verification of the OLPC strategy is presented in Section V. Finally, Section VI concludes this article.

## II. Basic Model of AH-VOC System

### A. AH-VOC System Description

The circuit and block diagram of the AH-VOC is shown in Fig. 1. $V_{\rm dc}$ represents the dc voltage, $L_f$ and $C_f$ are the filter inductance and capacitor, respectively. The grid impedance $Z_g$

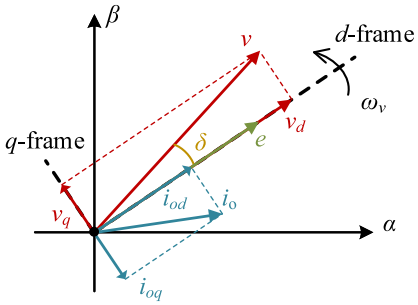


Fig. 2. Phasor diagram of AH-VOC connected to the grid.

represents the total impedance from the PCC and is donated by grid resistance $R_g$ and grid inductor $L_g$. $i$, $i_o$, $v$, and $e$ denote the converter-side current, grid-side current, filter capacitor voltage, and grid voltage, respectively.

The AH-VOC comprises two components: 1) a resonant $LC$ tank defining natural resonant frequency $\omega_{\rm n} = 1/\sqrt{LC}$; and 2) nonlinear state-dependent sources $v_m$ and $i_m$ to regulate energy exchange with the $LC$ circuit. Voltage and current scaling factors $k_v$ and $k_i$ are applied when connecting to the grid. The dynamics of $v_c$ and $i_L$ are governed by

$$\begin{cases} C\dot{v}_C = -i_L + i_m - u_1 \\ L\dot{i}_L = v_C + v_m - \xi u_2 \end{cases} \tag{1}$$

where $v_m = \mu(2Y_n^2 - \|y\|^2)y_2/\omega_n$, and $i_m = \mu(2Y_n^2 - \|y\|^2)y_1/\xi\omega_n$. Here, $\mu$ is the convergence speed, $y = [y_1, y_2]^T = [v_C, \xi i_L]^T$, and $\xi = \sqrt{L/C}$. The control inputs $u_1$, $u_2$ are determined from the difference between grid-side current $i_{\alpha\beta}$ and its setpoints $i^\star_{\alpha\beta}$, as follows:

$$\begin{bmatrix} u_1 \\ u_2 \end{bmatrix} = k_i \begin{bmatrix} \cos\sigma & -\sin\sigma \\ \sin\sigma & \cos\sigma \end{bmatrix} \begin{bmatrix} i_\alpha - i^\star_\alpha \\ i_\beta - i^\star_\beta \end{bmatrix} \tag{2}$$

where $\sigma$ facilitates the steady-state droop laws. With $\sigma = \pi/2$, frequency active power and voltage reactive power trade-offs are obtained. The output voltage $v_\alpha$, $v_\beta$ are expressed via $v_C$, $i_L$ and $k_v$ as

$$\begin{bmatrix} \dot{v}_\alpha \\ \dot{v}_\beta \end{bmatrix} = \begin{bmatrix} \frac{\mu}{k_v^2}\left(2V_{\rm n}^2 - 2V^2\right) & -\omega_{\rm n} \\ \omega_{\rm n} & \frac{\mu}{k_v^2}\left(2V_{\rm n}^2 - 2V^2\right) \end{bmatrix} \begin{bmatrix} v_\alpha \\ v_\beta \end{bmatrix} - \frac{k_v k_i}{C} \begin{bmatrix} i^\star_\beta - i_\beta \\ i_\alpha - i^\star_\alpha \end{bmatrix} \tag{3}$$

where $V = \sqrt{v_\alpha^2 + v_\beta^2}$. The dynamics of $V$ and $\delta$ can be written in polar coordinates as follows:

$$\begin{cases} \dot{V} = \frac{\mu}{k_v^2} V\left(2V_{\rm n}^2 - 2V^2\right) - \frac{k_v k_i}{3CV}\left(Q - Q_{\rm r}\right) \\ \omega = \omega_{\rm n} - \frac{k_v k_i}{3CV^2}\left(P - P_{\rm r}\right) \end{cases} \tag{4}$$

where $V_{\rm n}$ is the nominal voltage set-point, $P_{\rm r}$, $Q_{\rm r}$ are the reference active and reactive power, and $P$, $Q$ represent the actual values.

With grid voltage aligned to the $d$-axis, Fig. 2 illustrates the phasor diagram. The converter's linear model transforms into

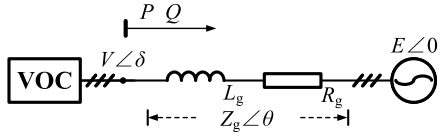


Fig. 3. Simplified circuit of AH-VOC system.

the $dq$-frame as

$$L_g\dot{\mathbf{i}}_{odq} = -R_g\mathbf{i}_{\mathbf{odq}} - j\omega L_g\mathbf{i}_{\mathbf{odq}} + \mathbf{v}_{\mathbf{dq}} - \mathbf{e} \tag{5}$$

where $\mathbf{i}_{\mathbf{odq}}$, $\mathbf{v}_{\mathbf{dq}}$, and $\mathbf{e}$ represent the $dq$ components of $i_o$, $v_o$, and $e$, respectively. The active power $P$ and reactive power $Q$ are expressed as

$$\begin{bmatrix} P \\ Q \end{bmatrix} = \frac{3}{2}\begin{bmatrix} v_d & v_q \\ v_q & -v_d \end{bmatrix}\begin{bmatrix} i_{od} \\ i_{oq} \end{bmatrix}. \tag{6}$$

Inner loops tracking voltage reference from (4). Large control bandwidths enable AH-VOC decoupling with inner loops in the low-frequency range. Therefore, the simplified circuit (Fig. 3) includes grid voltage $E\angle 0$, output voltage $V\angle\delta$, and line impedance $Z_g\angle\theta$.

### B. Small-Signal Model of AH-VOC System

As shown in Fig. 3, the output power of AH-VOC can be expressed as

$$\begin{cases} P = \frac{3V^2}{2Z_g}\cos\theta - \frac{3VE}{2Z_g}\cos(\delta+\theta) \\ Q = \frac{3V^2}{2Z_g}\sin\theta - \frac{3VE}{2Z_g}\sin(\delta+\theta) \end{cases} \tag{7}$$

where the power angle $\delta$ can be expressed as $\int(\omega - \omega_g)dt$, $\omega_g$ represents the angular frequency of the grid voltage.

The Jacobian matrix of the power flows is obtained by taking partial derivatives of $\delta$, $V$, and $E$ for active and reactive power, respectively, as

$$M = \begin{bmatrix} M_{11} & M_{12} & M_{13} \\ M_{21} & M_{22} & M_{23} \end{bmatrix} = \begin{bmatrix} \frac{\partial P}{\partial\delta} & \frac{\partial P}{\partial V} & \frac{\partial P}{\partial E} \\ \frac{\partial Q}{\partial\delta} & \frac{\partial Q}{\partial V} & \frac{\partial Q}{\partial E} \end{bmatrix}$$
$$= \begin{bmatrix} \frac{3V_0E_0}{2Z_g}\sin(\delta_0+\theta) & -\frac{3V_0E_0}{2Z_g}\cos(\delta_0+\theta) \\ \frac{3V_0}{Z_g}\cos\theta - \frac{3E_0}{2Z_g}\cos(\delta_0+\theta) & \frac{3V_0}{Z_g}\sin\theta - \frac{3E_0}{2Z_g}\sin(\delta_0+\theta) \\ -\frac{3V_0}{2Z_g}\cos(\delta_0+\theta) & -\frac{3V_0}{2Z_g}\sin(\delta_0+\theta) \end{bmatrix}^T \tag{8}$$

where subscript 0 denotes equilibrium, and the equilibrium state $x$ is derived from (4)–(6) as

$$x = [v_d, v_q, i_{od}, i_{oq}]^T. \tag{9}$$

Thus, the small signal model of (7) can be expressed as

$$\begin{cases} \hat{P} = M_{11}\hat{\delta} + M_{12}\hat{V} + M_{13}\hat{E} \\ \hat{Q} = M_{21}\hat{\delta} + M_{22}\hat{V} + M_{23}\hat{E} \\ \hat{\delta} = \frac{\hat{\omega}-\hat{\omega}_g}{s}. \end{cases} \tag{10}$$

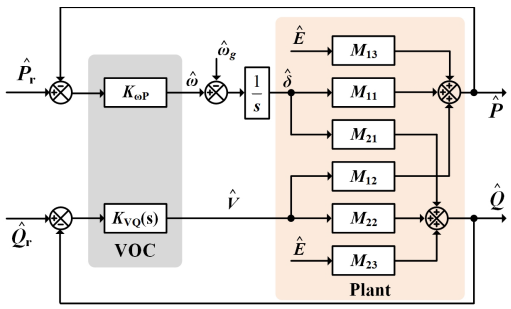


Fig. 4. Small-signal diagram of AH-VOC system.

According to (4), the small-signal linearized model of the AH-VOC can be obtained by neglecting higher-order terms

$$\begin{cases} \hat{V} = \frac{2\mu\left(V_n^2-3V_0^2\right)}{k_v^2}\hat{V} + \frac{k_v k_i (Q_0-Q_r)}{3CV_0^2}\hat{V} + \frac{k_v k_i}{3CV_0^2}\hat{Q}_r \\ \hat{\omega} = \frac{k_v k_i}{3CV_0^2}\hat{P}_r \end{cases} \tag{11}$$

where $V_0$ and $Q_0$ are the steady-state values.

By employing steady-state variables, the open-loop transfer function of the active power loop ($K_{\omega P}$) and reactive power loop ($K_{VQ}(s)$) can be obtained from (11) as follows:

$$K_{VQ}(s) = \frac{1}{as+b}, \quad K_{\omega P} = \frac{1}{c} \tag{12}$$

where

$$\begin{cases} a = \frac{3CV_0}{k_v k_i} \\ b = \frac{18\mu CV_0^3}{k_v^3 k_i} - \frac{6\mu CV_n V_0}{k_v^3 k_i} - \frac{Q_0-Q_r}{V_0} \\ c = \frac{3CV_0^2}{k_v k_i}. \end{cases} \tag{13}$$

The small-signal model from the references and disturbances to output (Fig. 4), derived from (10) and (12). This model reveals the wide-frequency power control model of AH-VOC, with $M_{21}$ and $M_{12}$ representing the active-reactive and reactive-active coupling paths, respectively.

## III. Wide-Frequency Power Control Analysis and OLPC Strategy

This section develops a CTFA for power control and robustness analysis, exposing the limitations of the virtual inductor method in steady-state decoupling, dynamic decoupling, and reactive power tracking. To address these limitations, an OLPC strategy is proposed, achieving enhanced decoupling and reactive power tracking accuracy across wide frequencies. Subsequently, comprehensive design procedures and bandwidth specifications are presented.

### A. Wide-Frequency Power Control Analysis

As shown in Fig. 4, power coupling is related not only to the plant but also to the AH-VOC. First, the RGA for analyzing multiinput multioutput systems can be expressed as

$$\Lambda = \Gamma \odot (\Gamma^{-1})^{\mathrm{T}} \tag{14}$$

where $\odot$ denotes the Hadamard product, which refers to the element-wise multiplication of corresponding matrix elements, and $\Gamma$ is the matrix of first amplification factors. Each element $\gamma_{ij}$ in $\Gamma$ is defined as

$$\gamma_{ij} = \left.\frac{\partial y_i}{\partial u_j}\right|_{u_k=\text{const},k\neq j} \tag{15}$$

where $y_i$ and $u_j$ representing the $i$th output and $j$th input, respectively.

The power control can be modeled as a two-input, two-output system, $\Gamma$ can be expressed as

$$\Gamma = \begin{bmatrix} \gamma_{11} & \gamma_{12} \\ \gamma_{21} & \gamma_{22} \end{bmatrix} = \begin{bmatrix} K_{\delta P}(s)M_{11} & K_{VQ}(s)M_{12} \\ K_{\delta P}(s)M_{21} & K_{VQ}(s)M_{22} \end{bmatrix} \tag{16}$$

where $K_{\delta P}(s) = K_{\omega P}/s$.

By substituting (16) into (14), $\Lambda$ is obtained as

$$\Lambda = \begin{bmatrix} \lambda_{11} & \lambda_{12} \\ \lambda_{21} & \lambda_{22} \end{bmatrix} = \frac{\begin{bmatrix} M_{11}M_{22} & -M_{12}M_{21} \\ -M_{12}M_{21} & M_{11}M_{22} \end{bmatrix}}{M_{11}M_{22} - M_{12}M_{21}}. \tag{17}$$

It is noteworthy that each row and column of $\Lambda$ sum to 1. When $\lambda_{11}$ approaches 1 or $\lambda_{12}$ approaches 0, the power coupling weakens. However, (17) is formulated under open-loop conditions, thereby inherently excluding the ability to rigorously assess the influence of closed-loop feedback mechanisms. To address this, a CTFA is developed to analyze power control considering power feedback. Assuming disturbances are applied to the power references and grid voltage/frequency, a CTFA can be derived using Mason's gain formula

$$\begin{aligned} S_{11}(s) &= K_{\delta P}(s)M_{11} + K_{\delta P}(s)K_{VQ}(s)M_{11}M_{22} \\ &\quad - K_{\delta P}(s)K_{VQ}(s)M_{12}M_{21} \\ S_{12}(s) &= K_{VQ}(s)M_{12}, S_{13}(s) = M_{13}(1 + K_{VQ}(s)M_{22}) \\ S_{14}(s) &= (M_{21}K_{VQ}(s)M_{12} - M_{11}(1 + K_{VQ}(s)M_{22}))/s \\ S_{21}(s) &= K_{\delta P}(s)M_{21} \\ S_{22}(s) &= K_{VQ}(s)M_{22} + K_{\delta P}(s)K_{VQ}(s)M_{11}M_{22} \\ &\quad - K_{\delta P}(s)K_{VQ}(s)M_{12}M_{21} \\ S_{23}(s) &= M_{23}(1 + K_{\delta P}(s)M_{11}), S_{24}(s) = -M_{21}/s \\ \Delta &= 1 + K_{\delta P}(s)M_{11} + K_{VQ}(s)M_{22} \\ &\quad + K_{\delta P}(s)K_{VQ}(s)M_{11}M_{22} \\ &\quad - K_{\delta P}(s)K_{VQ}(s)M_{12}M_{21} \end{aligned} \tag{18}$$

where $S_{ij}$ denotes the sum of the products of the forward path from the $i$th input to the $j$th output and the cofactor of the corresponding structure diagram, while $\Delta$ represents the characteristic function of the flow diagram. Therefore, the CTFA can be expressed as

$$\begin{aligned} T(s) &= \begin{bmatrix} T_{11}(s) & T_{12}(s) & T_{13}(s) & T_{14}(s) \\ T_{21}(s) & T_{22}(s) & T_{23}(s) & T_{24}(s) \end{bmatrix} \\ &= \frac{1}{\Delta}\begin{bmatrix} S_{11}(s) & S_{12}(s) & S_{13}(s) & S_{14}(s) \\ S_{21}(s) & S_{22}(s) & S_{23}(s) & S_{24}(s) \end{bmatrix}. \end{aligned} \tag{19}$$

TABLE I
MAIN PARAMETERS OF THE AH-VOC SYSTEM

| Parameters | Values | Parameters | Values |
|---|---|---|---|
| $P_{\rm n}$ | 5 kW (1 p.u.) | $L_f$ | 3 mH (0.13 p.u.) |
| $V_{\rm n}$ | 110 V (1 p.u.) | $C_f$ | 12 $\mu$F (0.0274 p.u.) |
| $I_{\rm n}$ | 15.15 A (1 p.u.) | $L_g$ | 5 mH (0.216 p.u.) |
| $\omega_{\rm n}$ | 100$\pi$ rad/s (1 p.u.) | $R_g$ | 3.2 $\Omega$ (0.441 p.u.) |
| $Z_{\rm n}$ | 7.26 $\Omega$ (1 p.u.) | $C$ | 0.0679 F |
| $V_{\rm dc}$ | 400 V | $\mu$ | 13 1/s$V^2$ |

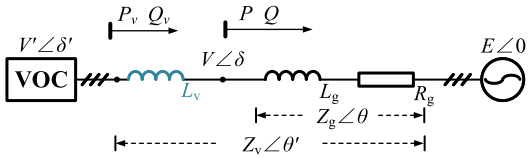


Fig. 5. Simplified circuit of AH-VOC system with a virtual inductor.

The CTFA elements convey clear physical meanings. Transfer functions $T_{11}(s)$ and $T_{22}(s)$ govern active and reactive power tracking performance, respectively, where $T_{22}(s) \approx 1$ ensures accurate reference tracking (e.g., 5 kvar $\Delta Q_{\rm r}$ yields 5 kvar output). Cross-coupling dynamics are quantified through $T_{12}(s)$ and $T_{21}(s)$, with $T_{12}(s) \approx 0$ indicating negligible active power coupling, while $T_{21}(s)$ values reflect reactive power coupling degree. For instance, $T_{21} = 0.2$ p.u. signifies that a 5 kW $\Delta P_{\rm r}$ step induces 1 kvar $\Delta Q$ . Voltage disturbance rejection is characterized by $T_{13}(s)$ and $T_{23}(s)$, where values near zero indicate robustness (e.g., 1.1V steps producing 50 W/var disturbances at 1 p.u.). similarly, $T_{14}(s)$ and $T_{24}(s)$ represent frequency disturbance attenuation, with small values signifying superior rejection (0.5 Hz steps causing 50 W/var disturbances at 1 p.u.). The CTFA with power feedback enables precise wide-frequency power analysis. Analysis covers 0–20 Hz due to low-pass characteristics, validated experimentally.

The wide-frequency power control of the virtual inductor method is evaluated using the above methods, with the main parameters listed in Table I. As shown in Fig. 5, the output power with a virtual inductor (VI) $L_v$ are expressed as

$$P = P_v, \quad Q = Q_v - \frac{3I^2\omega L_v}{2} \tag{20}$$

where $I$ is the amplitude of current, $P_v$ and $Q_v$ are the output power from $V'\angle\delta'$.

The Jacobian matrix of power flows can be expressed as

$$M_v = \begin{bmatrix} M_{v11} & M_{v12} \\ M_{v21} & M_{v22} \end{bmatrix} = \begin{bmatrix} \frac{\partial P}{\partial \delta'} & \frac{\partial P}{\partial V'} \\ \frac{\partial Q}{\partial \delta'} & \frac{\partial Q}{\partial V'} \end{bmatrix} = \begin{bmatrix} \frac{3V_0'E}{2Z_v}\sin(\delta_0' + \theta') & \frac{3E}{Z_v}\cos\theta' - \frac{3V_0'}{2Z_v}\cos(\delta_0' + \theta') \\ \frac{3V_0'E}{2Z_v}\cos(\delta_0' + \theta') & \frac{3V_0'}{Z_v}\sin\theta' - \frac{3E}{2Z_v}\sin(\delta_0' + \theta') \end{bmatrix} \tag{21}$$

where $Z_v\angle\theta'$ represents the total impedance (including $L_v$).

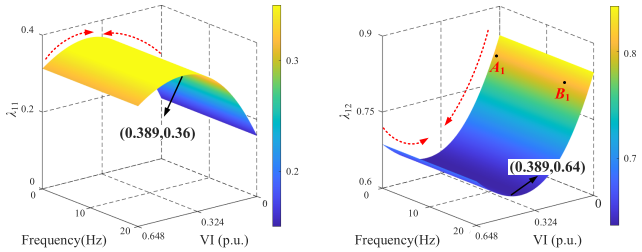


Fig. 6. Bode diagrams of the RGA for different $L_v$. (a) $\lambda_{11}(s)$. (b) $\lambda_{12}(s)$.

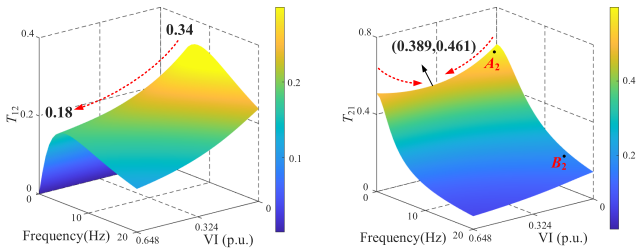


Fig. 7. Bode diagrams of the CTFA for different $L_v$. (a) $T_{12}(s)$. (b) $T_{21}(s)$.

Fig. 6 presents the bode diagrams of RGA for different $L_v$ (absolute magnitude). Optimal decoupling performance ($\lambda_{11} = 0.36$) occurs at $L_v = 0.389$ p.u. [Fig. 6(a)] with deviations increasing power coupling. However, the frequency independence of $\lambda_{11}$ and $\lambda_{12}$ limits the ability of RGA to characterize dynamics coupling effects.

Fig. 7 shows the bode diagrams of $T_{12}(s)$ and $T_{21}(s)$ for different $L_v$. $T_{21}(0) = 0$ indicates negligible active power coupling due to the integrator in the active loop. $T_{12}$ peaks at 10 Hz ranging from 0.34 to 0.18 p.u. Nonzero $T_{21}(0)$ [Fig. 7(b)] confirms $L_v$-dependent steady-state coupling, which is minimized at $L_v = 0.389$ p.u. (0.461 p.u.).

Figs. 6 and 7 reveal pronounced frequency-dependent coupling: the RGA cannot assess nonzero frequencies behavior, whereas the CTFA accurately captures it. Accordingly, we select points $A_1$-$A_2$ (0.689 Hz) and $B_1$-$B_2$ (15.17 Hz) to compare RGA and CTFA under $L_v = 0.033$ p.u. The theoretical coupling magnitudes are 0.807 at $A_1/B_1$, 0.578 p.u. at $A_2$, and 0.177 p.u. at $B_2$ . The results shows dynamic coupling cannot be captured by RGA but is quantified by CTFA. As shown in Fig. 8, a 0.2 p.u. perturbation at 0.689 Hz and 15.17 Hz is added to $P_{\rm r}$ at $t_1$. The measured reactive power responses, $\Delta Q_1 = 0.12$ p.u. and $\Delta Q_2 = 0.033$ p.u., closely match the CTFA predictions (0.116 p.u. and 0.035 p.u.), refuting the constantcoupling assumption of RGA and demonstrating the superiority for wide frequency coupling analysis of the CTFA.

Fig. 9 shows the bode diagrams of $T_{22}(s)$. At $L_v = 0$ p.u., $T_{22}$ peaks at 0.33 p.u. As $L_v$ decreases, the reactive power tracking is limited to approximately 0.2 p.u. As the frequency increases, the aforementioned trend remains consistent with that at 0 Hz.

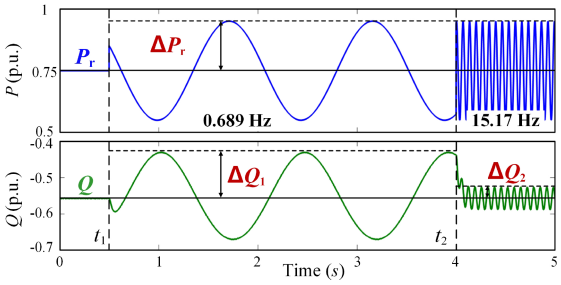


Fig. 8. Simulation validation of frequency-dependent power coupling characteristics.

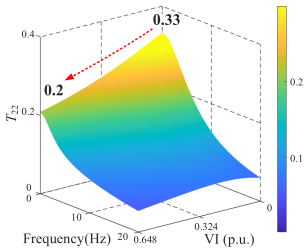


Fig. 9. Bode diagrams of the $T_{22}(s)$ for different $L_v$.

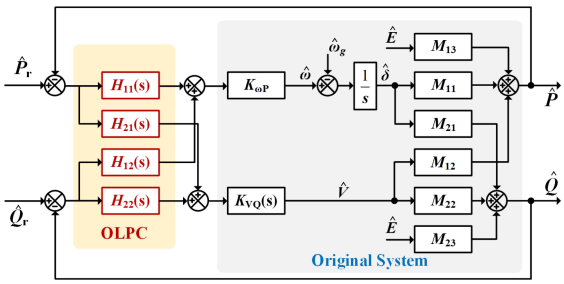


Fig. 10. Small-signal diagram of AH-VOC system with proposed OLPC strategy.

Consequently, the CTFA reveals that while increasing $L_v$ enhanced power decoupling, it degrades reactive power tracking, revealing a limitation of the virtual inductor method.

In conclusion, the CTFA provides a comprehensive quantification of closed-loop power control dynamics that the RGA fails to capture. It reveals a nonmonotonic steady-state relationship with $L_v$ (minimum at $L_v = 0.389$ p.u.) and $L_v$-dependent tradeoffs between power decoupling and reactive power tracking. Therefore, achieving wide-frequency power decoupling and accurate reactive power control remains a critical challenge.

### B. OLPC Control Structure

The OLPC ensures accurate and rapid power tracking and wide-frequency power decoupling in AH-VOC-controlled inverters. The power dynamics of inverters are modeled via a two-input, two-output transfer function matrix $\Gamma$. Integrated between the power error and AH-VOC (Fig. 10), the OLPC employs a proportional-integral (PI) controller $k_p + k_i/s$, satisfying the internal model principle for zero steady-state error. Hence, the OLPC can expressed as

$$H(s) = \varsigma \Psi^T(s) \tag{22}$$

where

$$\varsigma = \begin{bmatrix} \varsigma_{p,11} & \varsigma_{i,11} & \varsigma_{p,12} & \varsigma_{i,12} \\ \varsigma_{p,21} & \varsigma_{i,21} & \varsigma_{p,21} & \varsigma_{i,22} \end{bmatrix},$$
$$\Psi(s) = \begin{bmatrix} 1 & \frac{1}{s} & 0 & 0 \\ 0 & 0 & 1 & \frac{1}{s} \end{bmatrix}. \tag{23}$$

The power control model can be reformulated in frequency-domain as

$$L(j\omega) = \Gamma(s)\varsigma\Psi^T(s) = \begin{bmatrix} L_{11}(j\omega,\varsigma) & L_{12}(j\omega,\varsigma) \\ L_{21}(j\omega,\varsigma) & L_{22}(j\omega,\varsigma) \end{bmatrix}. \tag{24}$$

### C. Convex Optimization-Based OLPC Design

To achieve wide-frequency power decoupling and accurate reactive power control, the OLPC transfer function is designed with the following two objectives.

1) *Steady-state and dynamic power decoupling:* Ensure the nondiagonal terms of the transfer function vanish (zero gain) across the target frequency range.
2) *Fast and accurate power control:* Embed integral terms in diagonal elements and ensured compliance with the desired crossover frequency.

Following the guideline [30], the outer loop crossover frequency is typically set to one-fifth to one-tenth of the inner loop crossover frequency. Active and reactive power loop bandwidths are set to 25 and 60 Hz, corresponding to the switching frequency $f_s = 20$ kHz. Thus, $L_d(s)$ is derived as

$$L_d(s) = \begin{bmatrix} L_{d_1}(s) & 0 \\ 0 & L_{d_2}(s) \end{bmatrix} = \begin{bmatrix} \frac{50\pi}{s} & 0 \\ 0 & \frac{120\pi}{s} \end{bmatrix}. \tag{25}$$

To shape the control loop according to the desired transfer function, the OLPC design is formulated as a parameter optimization problem

$$\min_{\varsigma} \|L(\varsigma, s) - L_d(s)\|_2^2 \tag{26}$$

where $\|\cdot\|_2^2$ denotes the two-norm. The optimization problem must be represented in the frequency domain

$$\min_{\varsigma} \left\|\Gamma(j\omega)\varsigma\Psi^T(j\omega) - L_d(j\omega)\right\|_2^2 \quad \forall\omega \in \mathrm{R}. \tag{27}$$

*Note:* The CTFA method is excluded from the optimization objective due to its inherent nonconvexity. Instead, it is employed as an independent validation method to evaluate closed-loop control performance.

By incorporating the Gershgorin circle theorem and the Nyquist stability criterion, the optimization problem must enforce the following constraints to ensure the stability of the closed-loop system:

$$|h_s(\omega,\varsigma)| - \frac{\mathbf{Re}([1 + L_{d_s}(-j\omega)][1 + L_{ss}(j\omega,\varsigma)])}{|1 + L_{d_s}(j\omega)|} < 0 \tag{28}$$

for $s = 1, 2$ where

$$h_1(\omega, \varsigma) = |L_{21}(j\omega, \varsigma)| \quad h_2(\omega, \varsigma) = |L_{12}(j\omega, \varsigma)|. \tag{29}$$

The optimization problem described above is a typical convex semiinfinite programming (SIP) problem in which, for $\omega > 0$, both the optimal objective and the stability constraints must be strictly satisfied. To solve the SIP problem, this article employs the approach from reference [31], which discretizes the frequency range into a grid, effectively transforming the SIP problem into a convex semidefinite programming (SDP) problem

$$\min_{\varsigma} \sum_{i=0}^{N} \left\| \Gamma(j\omega_i)\varsigma\Psi^T(j\omega_i) - L_d(j\omega_i) \right\|_F^2 \tag{30}$$

subject to

$$|L_{21}(j\omega_i, \varsigma)| - \frac{\mathbf{Re}\left\{[1 + L_{d_1}(-j\omega_i)][1 + L_{11}(j\omega_i, \varsigma)]\right\}}{|1 + L_{d_1}(j\omega_i)|} < 0$$

$$|L_{12}(j\omega_i, \varsigma)| - \frac{\mathbf{Re}\left\{[1 + L_{d_2}(-j\omega_i)][1 + L_{22}(j\omega_i, \varsigma)]\right\}}{|1 + L_{d_2}(j\omega_i)|} < 0 \tag{31}$$

where $i = 0, \ldots, N$, $\| \cdot \|_F^2$ denotes the Frobenius norm.

The YALMIP toolbox [32] and the MOSEK solver [33] are employed to solve the SDP problem and determine the optimal parameters $\varsigma_o$. Finally, by applying the parameters from Table I, (9), (10), (15), and (27) are substituted into (32) to solve for the controller parameters. Then, the OLPC is discretized using the zero-order hold (ZOH) method to match the discrete system, as follows:

$$H(z) = \begin{bmatrix} \frac{r_1 z - r_2}{z-1} & -r_3 \\ \frac{r_4 z - r_5}{z-1} & \frac{r_6 z - r_7}{z-1} \end{bmatrix} \tag{32}$$

where

$$\begin{aligned} r_1 &= 1.177444907251127 & r_2 &= 1.177444907223504 \\ r_3 &= 20.615867966925393 & r_4 &= 3.482908028778827 \\ r_5 &= 3.468350077258384 & r_6 &= 11.397127291439427 \\ r_7 &= 11.349489274605460. \end{aligned} \tag{33}$$

### D. Online Selection-Based OLPC Design

Inherent uncertainties from renewable generation induce significant grid impedance variations, which shift inverter operating points and degrade the performance of fixed-parameter controllers. To mitigate these effects, Fig. 11 presents an OLPC framework employing offline pre-calculation and online parameter selection, operating as follows:

1) *Offline Calculation:* Input data including line impedance, control parameters, rated power, and rated voltage. Define (25) based on bandwidth theory. Utilizing tools like the convex optimization objective function and generalized Nyquist stability constraints, solve for the OLPC controller $H(s)$. Subsequently, validate whether the designed controller meets the requirements by the CTFA method. If the requirements are satisfied, archive parameters in table. If not, adjust the control parameters [7] or desired transfer functions and repeat the optimization design process until the CTFA performance are met before storing the parameters.
2) *Online Selection:* Estimate the line impedance value in real-time. Based on this estimated value, retrieve and apply the corresponding optimal OLPC parameters from the pre-constructed offline selected table.

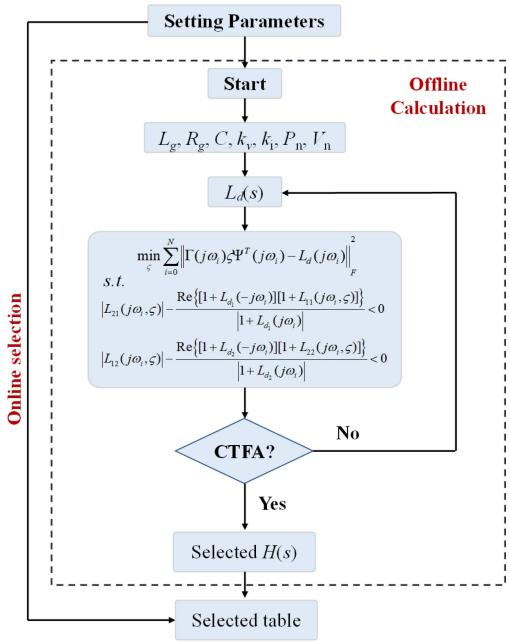


Fig. 11. Offline calculation and online selection framework.

*Remark:* While the proposed OLPC strategy optimizes single-inverter dynamics, its integration within hierarchical architectures enables parallel system operation. Power sharing is achieved through: 1) Power dispatch layer: Distributed algorithms (e.g., [34], [35]) compute power setpoints via communication networks; 2) Tracking layer: the OLPC strategy executes local control with wide-frequency power decoupling and accurate reactive power tracking.

## IV. Power Control Performance Analysis

This section validates the OLPC strategy under variable power references $P_r$ through two methods. The RGA evaluates power decoupling characteristics under open-loop conditions, while the CTFA quantifies wide-frequency power control dynamics considering power feedback. Furthermore, the reactive power tracking performance and robustness are validated by developed CTFA method.

### A. Steady-State Power Decoupling Analysis

As shown in Fig. 10, the first amplification factor with OLPC implemented is given as

$$\Gamma' = \begin{bmatrix} K_{\delta P}(s)M_{11} & K_{VQ}(s)M_{12} \\ K_{\delta P}(s)M_{21} & K_{VQ}(s)M_{22} \end{bmatrix} \begin{bmatrix} H_{11}(s) & H_{12}(s) \\ H_{21}(s) & H_{22}(s) \end{bmatrix}. \tag{34}$$

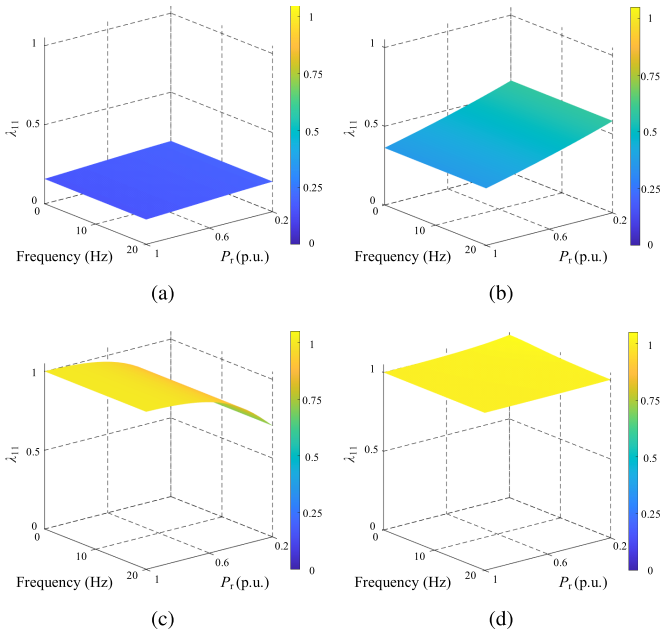


Fig. 12. Bode diagrams of the $\lambda_{11}$ for different $P_r$. (a) ND method. (b) OVI method. (c) QVPDC method. (d) OLPC strategy.

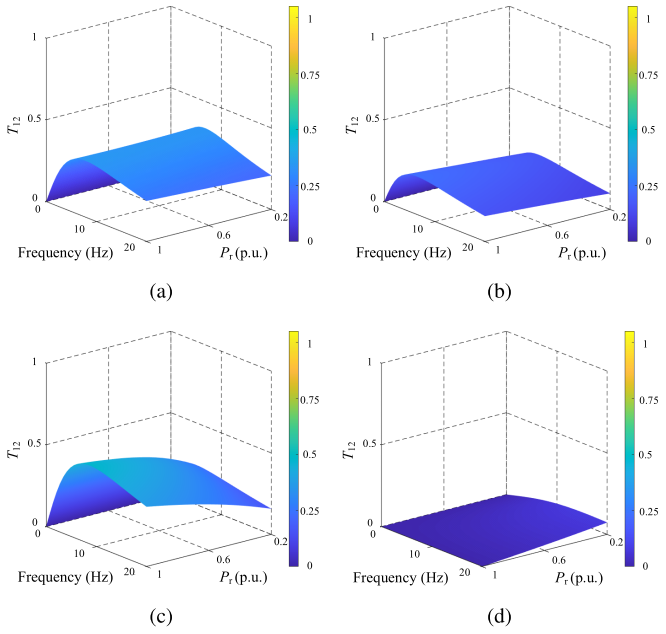


Fig. 13. Bode diagrams of the $T_{12}(s)$ for different $P_r$. (a) ND method. (b) OVI method. (c) QVPDC method. (d) OLPC strategy.

The bode diagrams of $\lambda_{11}$ calculated using (8), (12), (14), and (32) are shown in Fig. 12. Fig. 12(a)–(d) compare the no-decoupling (ND) method, optimal virtual inductor (OVI) method, QVPDC method [22], and proposed OLPC strategy. Closer $\lambda_{11}$ values to 1 indicates lower power coupling. For the ND method, $\lambda_{11}$ remains below 0.2 as $P_r$ decreases, reflecting severe coupling. The OVI method shows $\lambda_{11}$ rising from 0.36 to 0.58, indicating partial decoupling. The QVPDC method exhibits $\lambda_{11}$ decreasing from 1 to 0.7, demonstrating limited decoupling adaptability. In contrast, the OLPC strategy maintains $\lambda_{11} \approx 1$ across all $P_r$, validating its superior power decoupling capability.

### B. Wide-Frequency Power Decoupling Analysis

The $T'_{12}(s)$ and $T'_{21}(s)$ are simplified using Mason's gain formula as follows:

$$T'_{12}(s) = \frac{\rho_{12}}{\Delta'}, T'_{21}(s) = \frac{\rho_{21}}{\Delta'} \tag{35}$$

where

$$\begin{aligned}
\rho_{11} &= K_{\delta P}(s)M_{11}H_{11}(s) + K_{VQ}(s)M_{12}H_{21}(s) \\
\rho_{12} &= K_{\delta P}(s)M_{11}H_{12}(s) + K_{VQ}(s)M_{12}H_{22}(s) \\
\rho_{21} &= K_{\delta P}(s)M_{21}H_{11}(s) + K_{VQ}(s)M_{22}H_{21}(s) \\
\rho_{22} &= K_{\delta P}(s)M_{21}H_{12}(s) + K_{VQ}(s)M_{22}H_{22}(s) \\
\Delta' &= 1 + \rho_{11} + \rho_{22} - \rho_{12}\rho_{21} + \rho_{11}\rho_{22}.
\end{aligned} \tag{36}$$

Fig. 13 presents the bode diagrams of $T_{12}(s)$. While the OVI and QVPDC methods partially suppress dynamic active power coupling compared to the ND method, both exhibit degraded performance under variable amplitude and frequency of $P_r$. In contrast, the proposed OLPC strategy maintains $T_{12}$ below 0.074 p.u. and achieves complete decoupling, especially at $P_r = 1$ p.u.

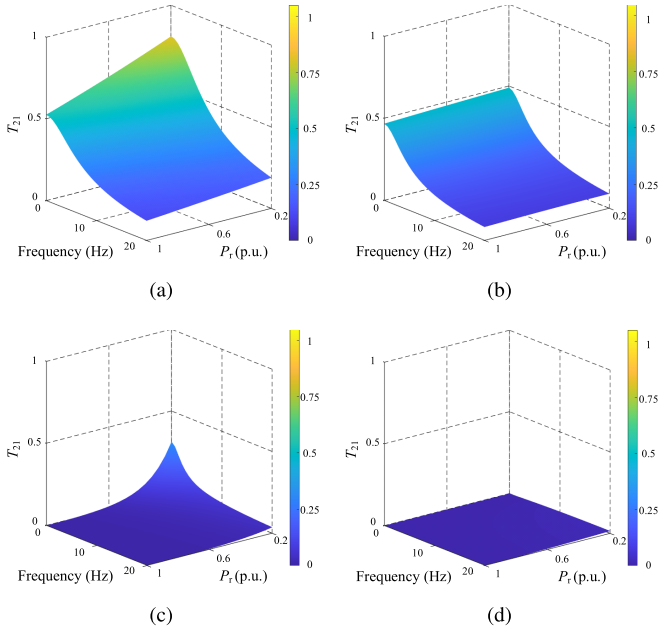


Fig. 14. Bode diagrams of the $T_{21}(s)$ for different $P_r$. (a) ND method. (b) OVI method. (c) QVPDC method. (d) OLPC strategy.

Fig. 14 shows the bode diagrams of $T_{21}(s)$. Compared to the ND method, the OVI method reduces reactive power coupling but exhibits increased coupling at lower $P_r$ without achieving complete decoupling. The QVPDC method provides adequate decoupling at $P_r = 1$ p.u., but $T_{21}$ rises to 0.31 p.u. under variable $P_r$. In contrast, the proposed OLPC strategy maintains $T_{21}$ below 0.015 p.u., effectively suppressing wide-frequency

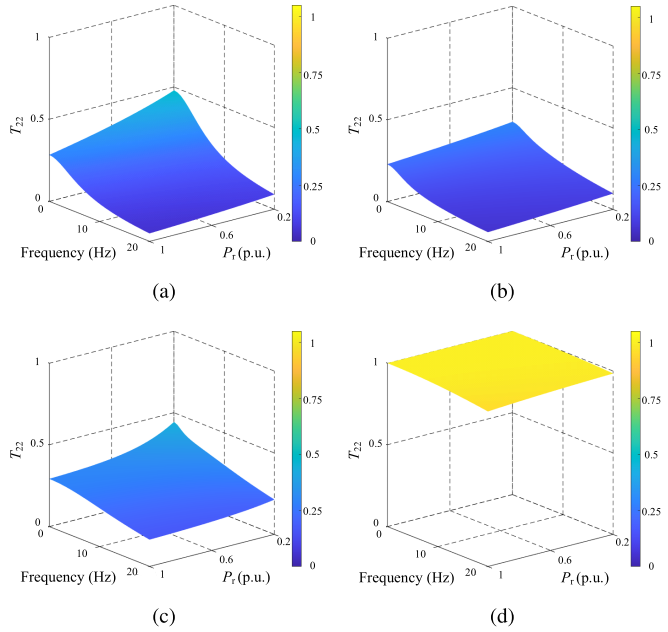


Fig. 15. Bode diagrams of the $T_{22}(s)$ for different $P_r$. (a) ND method. (b) OVI method. (c) QVPDC method. (d) OLPC strategy.

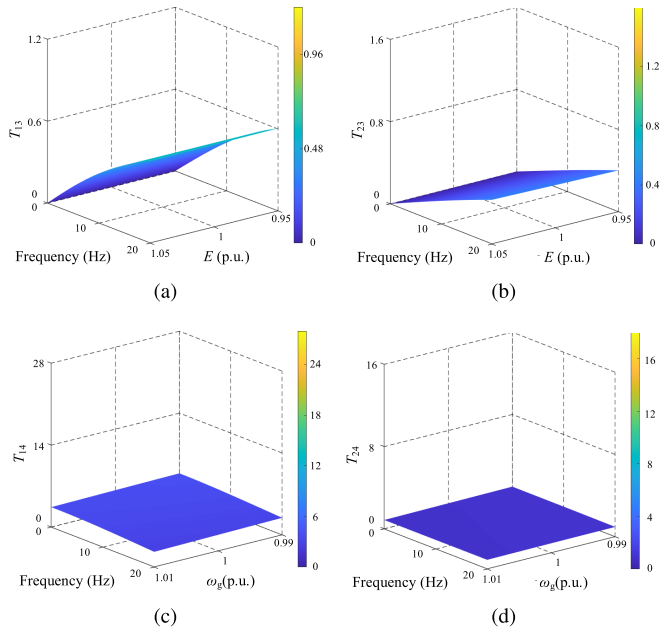


Fig. 16. Bode diagrams under grid disturbances. (a) $T_{13}(s)$. (b) $T_{23}(s)$. (c) $T_{14}(s)$. (d) $T_{24}(s)$.

reactive power coupling. Combined Fig. 13, these results confirm the superiority of the proposed OLPC strategy in achieving wide-frequency power decoupling across variable operating conditions.

### C. Reactive Power Tracking Analysis

The $T'_{22}(s)$ is simplified using Mason's gain formula as follows:

$$T'_{22}(s) = \frac{\rho_{22} + \rho_{11}\rho_{22} - \rho_{12}\rho_{21}}{\Delta'} \tag{37}$$

where $\rho_{22}$, $\rho_{22}$, $\rho_{22}$, $\rho_{22}$, and $\Delta'$ are given in (36).

Fig. 15 presents the bode diagrams of $T_{22}(s)$. The ND method exhibits the highest reactive power tracking accuracy, yet still falls below 0.5 p.u., indicating an inherent limitation in reactive power tracking. However, both the OVI and QVPDC methods demonstrate reduced reactive power tracking accuracy compared to the ND method, with the OVI method performing worse. Conversely, the proposed OLPC strategy not only achieves accurate reactive power reference tracking near the nominal operating point, but also maintains $T_{22} \approx 1$ p.u. across variable amplitude and frequency of $P_r$, validating its excellent reactive power tracking performance.

### D. Robust Analysis Against Gird Disturbances

The $T'_{13}(s)$, $T'_{23}(s)$, $T'_{14}(s)$, and $T'_{24}(s)$ are simplified using Mason's gain formula as follows:

$$T'_{13}(s) = \frac{M_{13}(1+\rho_{22})}{\Delta'}, T'_{23}(s) = \frac{M_{23}(1+\rho_{11})}{\Delta'}$$
$$T'_{14}(s) = \frac{M_{21}H_{22}(s)K_{VQ}(s)M_{12}}{\Delta' s}$$
$$- \frac{M_{11}(1+H_{22}(s)K_{VQ}(s)M_{22})}{\Delta' s}$$
$$T'_{24}(s) = \frac{-M_{21}(1+H_{21}(s)K_{VQ}(s)M_{12})}{\Delta' s} \tag{38}$$

where $\rho_{22}$, $\rho_{22}$, $\rho_{22}$, $\rho_{22}$, and $\Delta'$ are given in (36). $M_{11}$, $M_{12}$, $M_{21}$, and $M_{22}$ are given in (8). $H_{21}(s)$ and $H_{22}(s)$ are the OLPC transfer functions.

Fig. 16(a)–(b) depict the bode diagrams of $T_{13}(s)$ and $T_{23}(s)$ under $\pm$ 5% grid voltage variations with the proposed OLPC strategy. At steady-state, both transfer functions exhibits zero magnitude, confirming negligible impact on active and reactive power outputs. During frequency increasing, $T_{13}$ and $T_{23}$ maintain gain below 0.5 p.u., indicating strong rejection of voltage disturbance. Similarly, Fig. 16(c)–(d) show the bode diagrams of $T_{14}(s)$ and $T_{24}(s)$ under $\pm$ 1 % grid frequency variations. The proposed OLPC strategy limits $T_{14}$ gain below 6 p.u., while $T_{24}$ maintains a gain below 1 p.u. This demonstrates the robustness of the reactive power control against grid frequency disturbances. Consequently, the proposed OLPC strategy achieves excellent disturbance rejection for both grid voltage and grid frequency disturbances.

### E. Robust Analysis Under Strong Grid Condition

When the short-circuit ratio (SCR) is 7 ($L_g = 1$ mH (0.043 p.u.), $R_g = 1\Omega$ (0.138 p.u.)), the OLPC control parameters can be optimized by (25)–(31) based on the offline calculation and online selection framework. Then the OLPC is discretized using the ZOH method as follows:

$$H'(z) = \begin{bmatrix} \frac{r_8 z - r_9}{z-1} & -r_{10} \\ \frac{r_{11}z - r_{12}}{z-1} & \frac{r_{13}z - r_{14}}{z-1} \end{bmatrix} \tag{39}$$

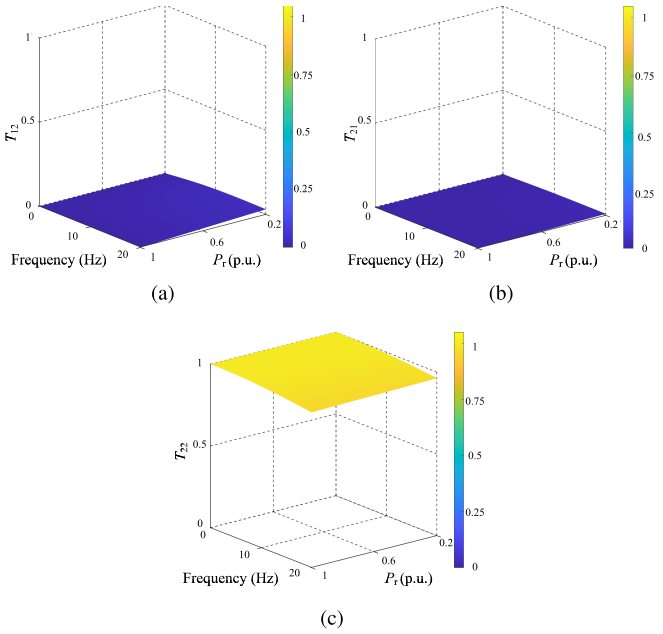


Fig. 17. Bode diagrams under strong grid condition (SCR = 7). (a) $T_{12}(s)$. (b) $T_{21}(s)$. (c) $T_{22}(s)$.

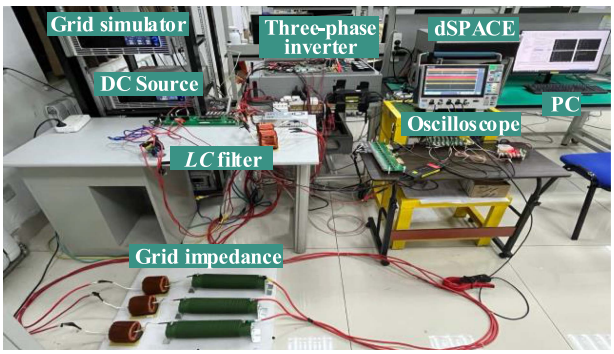


Fig. 18. Configuration of the experimental system prototype.

where

$$r_8 = 0.385857129637793 \qquad r_9 = 0.385857130289611$$
$$r_{10} = 4.072265369313690 \qquad r_{11} = 1.318430820195425$$
$$r_{12} = 1.313521287682836 \qquad r_{13} = 1.347356199411704$$
$$r_{14} = 1.342338956048231. \tag{40}$$

Fig. 17 presents the bode diagrams of the proposed OLPC strategy under strong grid conditions (SCR = 7). The strategy achieves complete steady-state active-reactive power decoupling ($T_{21}(0) = 0, T_{12}(0) = 0$) during power reference changes. Dynamic decoupling performance is significantly enhanced, with $T_{21}$ and $T_{12}$ magnitudes maintained below 0.1 p.u. Furthermore, accurate reactive power tracking is demonstrated through $T_{22} \approx 1$ p.u. across the operational frequency range.

In summary, the proposed OLPC strategy is validated through both conventional RGA and the developed CTFA to achieve not only wide-frequency active/reactive power decoupling, but also accurate reactive power tracking. Furthermore, the strategy demonstrates superior robustness under grid disturbances and strong grid conditions.

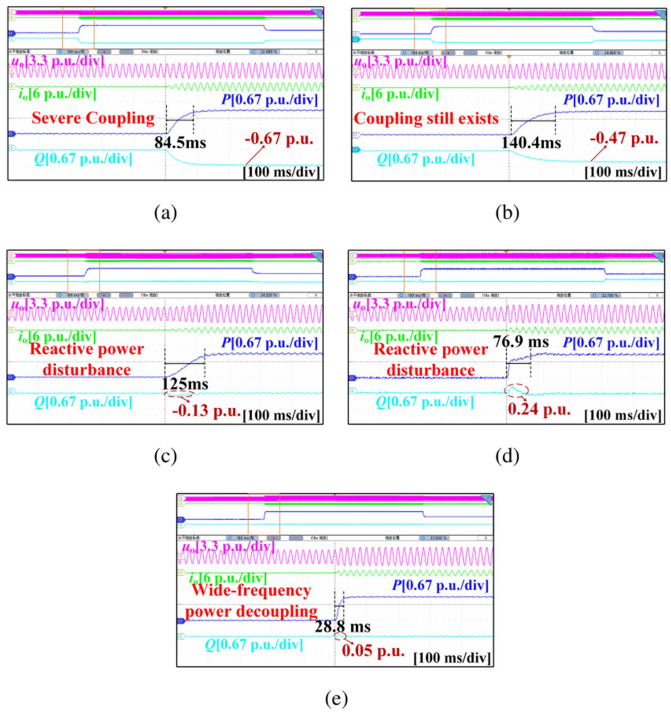


Fig. 19. Experimental waveforms in Case I. (a) ND method. (b) OVI method. (c) QVPDC method. (d) VPCCE method. (e) OLPC strategy.

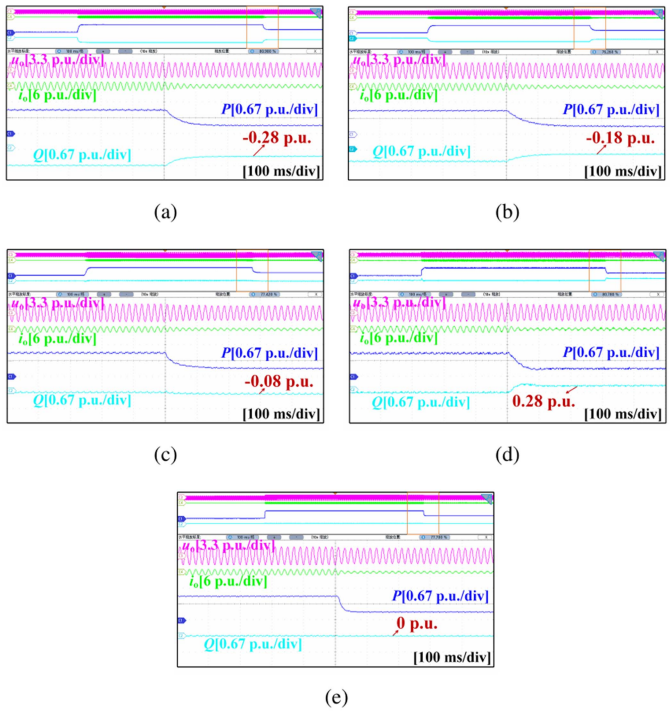


Fig. 20. Experimental waveforms in Case II. (a) ND method. (b) OVI method. (c) QVPDC method. (d) VPCCE method. (e) OLPC strategy.

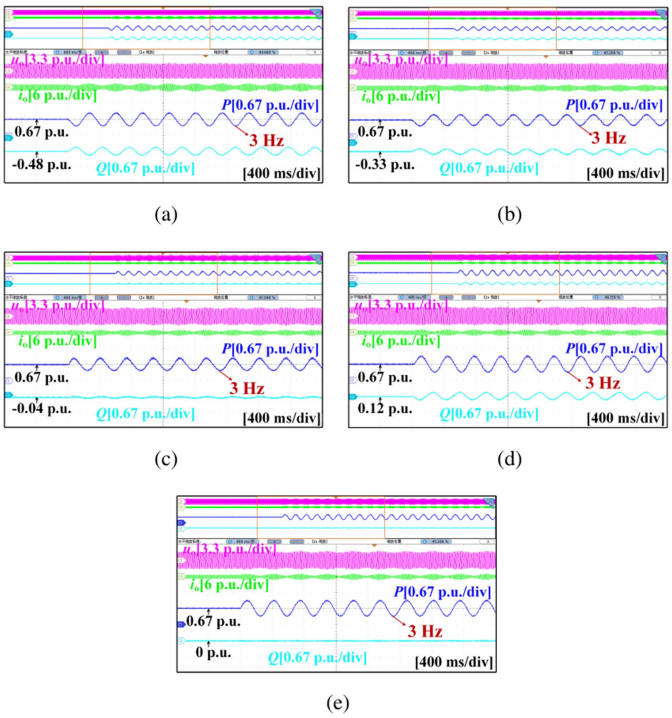


Fig. 21. Experimental waveforms in Case III. (a) ND method. (b) OVI method. (c) QVPDC method. (d) VPCCE method. (e) OLPC strategy

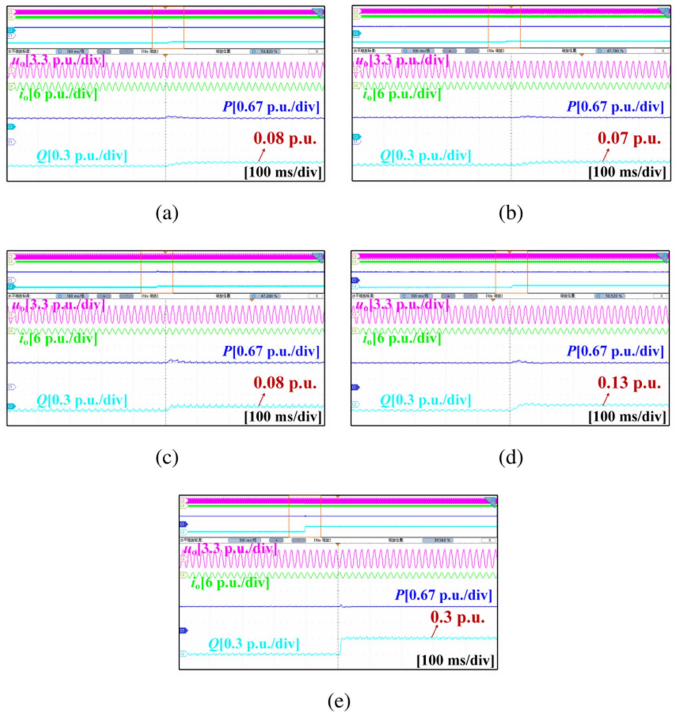


Fig. 22. Experimental waveforms in Case IV. (a) ND method. (b) OVI method. (c) QVPDC method. (d) VPCCE method. (e) OLPC strategy

## V. Experimental Verification

### A. Hardware Setup

The experiments are conducted by the hardware setup in Fig. 18, which comprises a three-phase inverter, an $LC$ filter, a digital control system (dSPACE DS6051), a dc power source (Chroma 62180D-1800), and an ac power source (Chroma 61815). The experimental setup parameters are listed in Table I in Section III. The grid impedance is configured with 3 Ω resistance and 5 mH inductance, creating strong coupling between power control loops.

In the experiment, the initial power references are given as $P_{\mathrm{r}} = 0$ p.u., $Q_{\mathrm{r}} = 0$ p.u. We compared five typical control schemes, including the ND method, OVI method, QVPDC method, VPCCE method, and OLPC strategy. For the OVI method, the optimal virtual inductance is set to 0.389 p.u, while for the QVPDC method, the decoupling virtual inductance is 1.09 p.u. [22]. The VPCCE method is guided by [15]. The following four scenarios were used for comparison.

$Case\ I$: $P_{\mathrm{r}}$ increases from 0 to 1 p.u. To guarantee a fair comparison, the virtual inductance is the optimal option in QVPDC and VI methods.

$Case\ II$: $P_{\mathrm{r}}$ decreases from 1 to 0.33 p.u., which is used to verify the adaptability at different working points.

$Case\ III$: A magnitude 0.33 p.u. and frequency 3 Hz ac disturbance is added to $P_{\mathrm{r}}$ under initial references $P_{\mathrm{r}} = 0.67$ p.u. and $Q_{\mathrm{r}} = 0$ p.u., which is used to demonstrate the dynamic decoupling performance.

$Case\ IV$: $Q_{\mathrm{r}}$ increase from 0 to 0.3 p.u.under initial references $P_{\mathrm{r}} = 1$ p.u. and $Q_{\mathrm{r}} = 0$ p.u., which is used to test the

### B. Experimental Results

Figs. 19–22 shows the experimental waveforms under four cases, which subfigures (a)–(e) corresponding to ND, OVI, QVPDC, VPCCE, and proposed OLPC methods.

*1) Steady-State Power Decoupling:* Fig. 19 shows the power waveforms with different methods in Case I. With the ND method, the reactive power $Q_0$ reaches $-0.67$ p.u., indicating severe steady-state power coupling. By applying the OVI method, the $Q_0$ can be reduced to $-0.47$ p.u., aligning with theoretical analysis. However, steady-state power coupling still exists. The QVPDC and VPCCE methods achieve steady-state power decoupling but induce large dynamic reactive power disturbances ($-0.13$ p.u., 0.24 p.u.). In contrast, the proposed OLPC strategy achieves steady-state decoupling with only 0.05 p.u. transient disturbance. The response time of ND method is 84.5 ms. The OVI and QVPDC methods increase response time to 140.4 ms and 125 ms, respectively, while VPCCE method reduces it to 76.9 ms. However, the OLPC strategy reduces response time to 28.8 ms.

*2) Adaptive Power Decoupling for $P_{\mathrm{r}}$ Variations:* Fig. 20 shows the power waveforms with different methods in Case II. When $P_{\mathrm{r}}$ decreases from 1 p.u. to 0.33 p.u., the $Q_0$ for the ND and OVI methods are $-0.28$ p.u. and $-0.18$ p.u., respectively. However, the OVI method still fails to achieve steady-state decoupling. For the QVPDC method, the $Q_0$ becomes $-0.08$ p.u., indicating its inability to $P_{\mathrm{r}}$ variations. Similarly, the $Q_0$ becomes 0.28 p.u. for the VPCCE method. In contrast, as illustrated in Fig. 20(e), the OLPC strategy maintains the $Q_0$ consistently at 0 p.u., showing the capability to accommodate in $P_{\mathrm{r}}$.

*3) Dynamic Power Decoupling:* Fig. 21 shows the power waveforms in Case III. The degree of dynamic coupling can

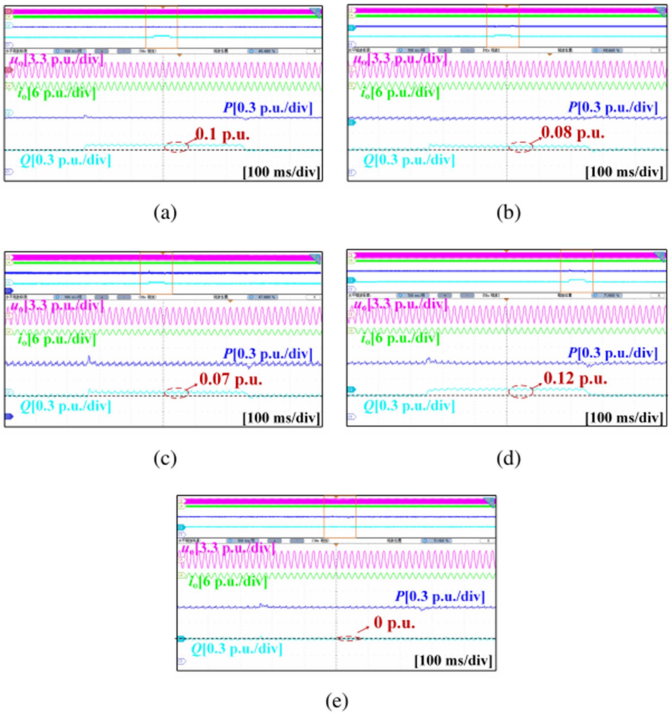


Fig. 23. Experimental waveforms under a 5% grid voltage sag. (a) ND method. (b) OVI method. (c) QVPDC method. (d) VPCCE method. (e) OLPC strategy.

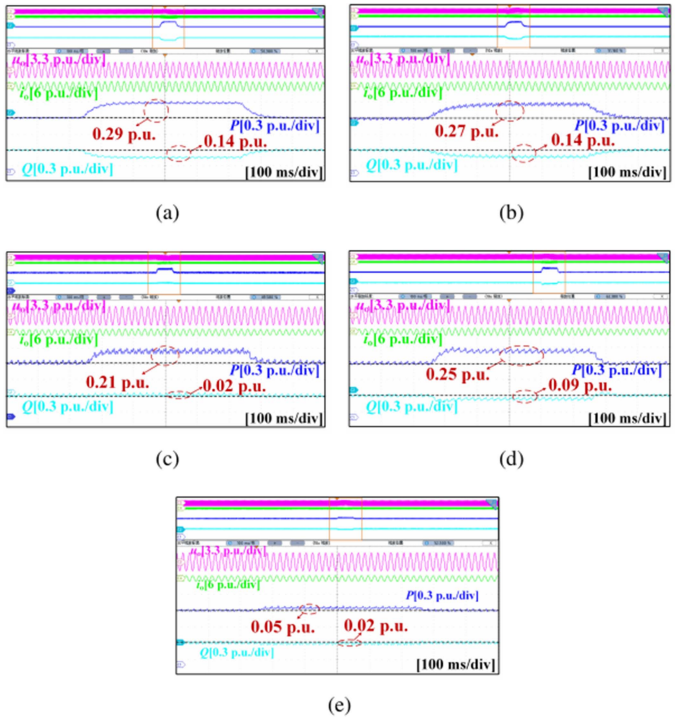


Fig. 24. Experimental waveforms under a 1% grid frequency reduction. (a) ND method. (b) OVI method. (c) QVPDC method. (d) VPCCEmethod. (e) OLPC strategy.

fluctuations at 3 Hz. The ND, OVI, and VPCCE methods show significant reactive power fluctuations, indicating poor dynamic power decoupling performance, while the QVPDC method exhibits smaller fluctuations. However, with the OLPC strategy, the reactive power fluctuations can be considered negligible, indicating effective dynamic decoupling control.

*4) Reactive Power Control:* Fig. 22 depicts the power waveforms with different methods in Case IV. While $Q_r$ steps to 0.3 p.u., $Q_0$ of ND, OVI, QVPDC, and VPCCE methods are 0.08 p.u., 0.07 p.u., 0.08 p.u., and 0.13 p.u., respectively. The VPCCE method performs best but none achieve accurate reactive power tracking. In contrast, the proposed OLPC strategy achieves 0.3 p.u. reactive power output, validating precise reactive power tracking.

*5) Robustness Against Grid Disturbances:* Fig. 23 depicts the power waveforms during a 5% grid voltage sag (500 ms), which subfigures (a)–(e) corresponding to ND, OVI, QVPDC, VPCCE, and proposed OLPC methods. All methods achieve active power recovery postsag, indicating unaffected active power control. Reactive power deviations occur in ND method (0.1 p.u.), OVI method (0.08 p.u.), QVPDC method (0.07 p.u.), and VPCCE method (0.12 p.u.), while OLPC strategy maintains full power decoupling. Similarly, Fig. 24 shows response to a 1% grid frequency reduction (500 ms). Significant active power deviations appear in ND (0.29 p.u.), OVI (0.27 p.u.), QVPDC (0.21 p.u.), and VPCCE (0.25 p.u.) methods, whereas the proposed OLPC strategy limits deviation to 0.05 p.u. Reactive power deviates by 0.14 p.u.(ND/OVI methods), 0.09 p.u. (VPCCE method), and 0.02 p.u. (QVPDC/OLPC methods). The minimal deviations validate the superior robustness of OLPC strategy against grid disturbances.

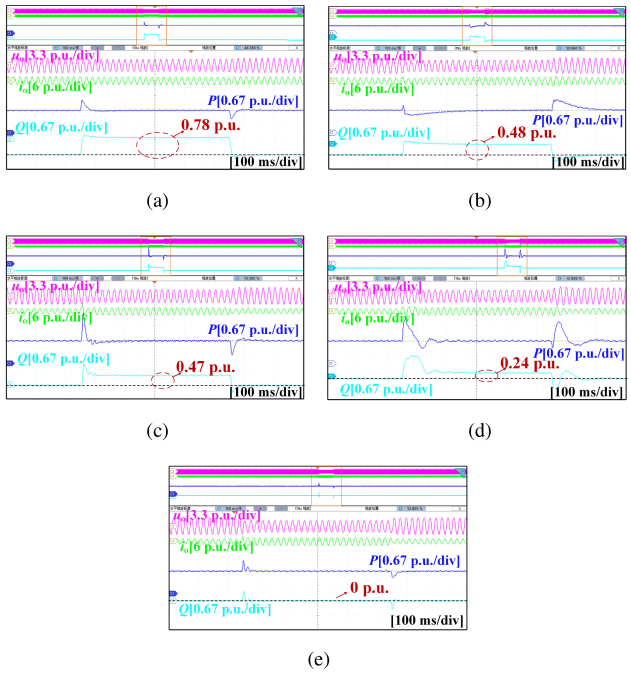


Fig. 25. Experimental waveforms under a grid fault. (a) ND method. (b) OVI method. (c) QVPDC method. (d) VPCCE method. (e) OLPC strategy.

*6) Robustness Under Grid Fault:* Fig. 25 presents the power waveforms during a 50% grid voltage sag (500 ms). Under this fault condition, significant reactive power coupling occurs in ND (0.78 p.u.), OVI (0.48 p.u.), QVPDC (0.47 p.u.), and VPCCE (0.24 p.u.) methods. Although OVI, QVPDC, and VPCCE reduce coupling compared to ND, none achieves power decoupling

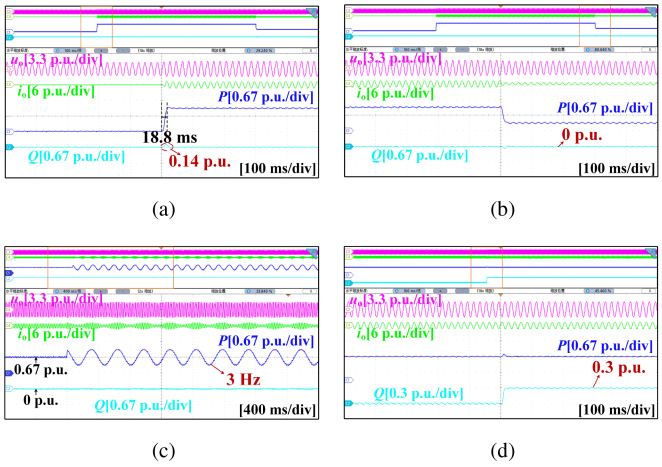


Fig. 26. Experimental waveforms under strong grid (SCR = 7). (a) Case I. (b) Case II. (c) Case III. (d) Case IV.

during faults. In contrast, the proposed OLPC strategy maintains exactly 0 p.u. reactive power output, demonstrating complete steady-state decoupling. These results validate the robustness of OLPC strategy under grid faults.

*7) Robustness Under Strong Grid Condition:* Fig. 26 shows the power waveforms under strong grid in four cases. For steady-state power decoupling, the proposed OLPC strategy achieves complete decoupling with a reactive power transient disturbance of only 0.14 p.u. And its response time is 18.8 ms. While $P_{\mathrm{r}}$ changes, the OLPC strategy maintain power decoupling. For dynamic power decoupling, reactive power disturbance remains near zero, demonstrating superior dynamic power decoupling performance. For reactive power tracking, the OLPC strategy achieves 0.3 p.u. reactive power output, validating accurate reactive power tracking. Therefore, the proposed OLPC strategy exhibits excellent performance under strong grid condition.

In conclusion, the CTFA provides rigorous analysis of wide-frequency power control and robustness against grid disturbances, incorporating power feedback dynamics. The proposed OLPC strategy effectively achieves wide-frequency power decoupling, rapid dynamic response, and precise reactive power regulation, demonstrating significant resilience to equilibrium point variations. Under grid disturbances and varying SCRs, the proposed OLPC strategy exhibits extremely robustness.

## VI. Conclusion

This article proposes an optimized loop-shaping-based power control method for AH-VOC based inverters. The proposed approach effectively addresses power coupling and reactive power control inaccuracies caused by AH-VOC control, $R/X$, and power angle across a power reference range of 0.2–1 p.u. and a frequency range of 0–20 Hz. By reformulating the loop-shaping problem as a convex optimization problem, the OLPC parameters are optimally designed. The strategy demonstrates approximate wide-frequency decoupling of active and reactive power control through RGA and CTFA analysis methods with rapid dynamic response. Reactive power control reshaping ensures accurate reactive power tracking. Furthermore, the OLPC strategy demonstrates better robustness against grid disturbances and maintains stable performance across varying SCRs. Experimental results confirm the superior performance of the OLPC strategy.

## References

[1] C. Li, S. K. Chaudhary, M. Savaghebi, J. C. Vasquez, and J. M. Guerrero, "Power flow analysis for low-voltage AC and DC microgrids considering droop control and virtual impedance," *IEEE Trans. Smart Grid*, vol. 8, no. 6, pp. 2754–2764, Nov. 2017.

[2] S. Kim, K.-H. Kim, S. Cui, and J.-J. Jung, "Adjustable virtual impedance via anti-windup method for enhancing transient stability and grid-forming capability under current limiting conditions," *IEEE Trans. Power Electron.*, vol. 40, no. 5, pp. 6423–6428, May 2025.

[3] N. Shabanikia and S. A. Khajehoddin, "Analysis and design of droop-controlled grid-forming inverters using novel WD agg approach," *IEEE Trans. Ind. Electron.*, vol. 71, no. 8, pp. 9110–9121, Aug. 2024.

[4] G. Heo, Y. Park, K. Lee, and H. Ryu, "A control method using two electromotive forces and a disturbance observer to improve the dynamics of a virtual synchronous machine," *IEEE Trans. Sustain. Energy*, vol. 15, no. 2, pp. 1050–1061, Apr. 2024.

[5] C. Arghir, T. Jouini, and F. Dörfler, "Grid-forming control for power converters based on matching of synchronous machines," *Automatica*, vol. 95, pp. 273–282, Sep. 2018.

[6] B. B. Johnson, M. Sinha, N. G. Ainsworth, F. Dorfler, and S. V. Dhople, "Synthesizing virtual oscillators to control islanded inverters," *IEEE Trans. Power Electron.*, vol. 31, no. 8, pp. 6002–6015, Aug. 2016.

[7] M. Lu, S. Dutta, V. Purba, S. Dhople, and B. Johnson, "A grid-compatible virtual oscillator controller: Analysis and design," in *Proc. Energy Convers. Congr. Expo.*, 2019, pp. 2643–2649.

[8] C. Shen, W. Gu, X. Shen, and Y. Xu, "Lyapunov method-based coherent aggregation of grid-forming converters for transient stability equivalents," *IEEE Trans. Smart Grid*, vol. 16, no. 2, pp. 1462–1479, Mar. 2025.

[9] L. Huang, H. Xin, Z. Wang, L. Zhang, K. Wu, and J. Hu, "Transient stability analysis and control design of droop-controlled voltage source converters considering current limitation," *IEEE Trans. Smart Grid*, vol. 10, no. 1, pp. 578–591, Jan. 2019.

[10] Z. Gong, C. Liu, L. Shang, Q. Lai, and Y. Terriche, "Power decoupling strategy for voltage modulated direct power control of voltage source inverters connected to weak grids," *IEEE Trans. Sustain. Energy*, vol. 14, no. 1, pp. 152–167, Jan. 2023.

[11] K. De Brabandere, B. Bolsens, J. Van Den Keybus, A. Woyte, J. Driesen, and R. Belmans, "A voltage and frequency droop control method for parallel inverters," *IEEE Trans. Power Electron.*, vol. 22, no. 4, pp. 1107–1115, Jul. 2007.

[12] Y. Li and Y. W. Li, "Power management of inverter interfaced autonomous microgrid based on virtual frequency-voltage frame," *IEEE Trans. Smart Grid*, vol. 2, no. 1, pp. 30–40, Mar. 2011.

[13] T. Wu, Z. Liu, J. Liu, S. Wang, and Z. You, "A unified virtual power decoupling method for droop-controlled parallel inverters in microgrids," *IEEE Trans. Power Electron.*, vol. 31, no. 8, pp. 5587–5603, Aug. 2016.

[14] C. N. Rowe, T. J. Summers, R. E. Betz, D. J. Cornforth, and T. G. Moore, "Arctan power–frequency droop for improved microgrid stability," *IEEE Trans. Power Electron.*, vol. 28, no. 8, pp. 3747–3759, Aug. 2013.

[15] B. Li, L. Zhou, X. Yu, C. Zheng, and J. Liu, "Improved power decoupling control strategy based on virtual synchronous generator," *IET Power Electron.*, vol. 10, no. 4, pp. 462–470, Mar. 2017.

[16] Y. Tian, X. Xu, Y. Wang, Z. Li, Z. Zhang, and Y. Gao, "Full-state feedback power decoupling control for grid forming converter with improved stability and inertia response," *IEEE Trans. Power Electron.*, vol. 40, no. 2, pp. 2930–2942, Feb. 2025.

[17] M. Li et al., "A novel virtual synchronous generator control strategy based on improved swing align emulating and power decoupling method," in *Proc. Energy Convers. Congr. Expo.*, 2016, pp. 1–7.

[18] B. Li and L. Zhou, "Power decoupling method based on the diagonal compensating matrix for VSG-Controlled parallel inverters in the microgrid," *Energies*, vol. 10, no. 12, 2017,, Art. no. 2159.

[19] J. M. Guerrero, L. GarciadeVicuna, J. Matas, M. Castilla, and J. Miret, "Output impedance design of parallel-connected UPS inverters with wireless load-sharing control," *IEEE Trans. Ind. Electron.*, vol. 52, no. 4, pp. 1126–1135, Aug. 2005.

[20] M. Li, Y. Wang, Y. Liu, N. Xu, S. Shu, and W. Lei, "Enhanced power decoupling strategy for virtual synchronous generator," *IEEE Access*, vol. 8, pp. 73601–73613, 2020.

[21] T. Wen, X. Zou, D. Zhu, X. Guo, L. Peng, and Y. Kang, "Comprehensive perspective on virtual inductor for improved power decoupling of virtual synchronous generator control," *IET Renew. Power Gen.*, vol. 14, no. 4, pp. 485–494, Mar. 2020.
[22] T. Wen, D. Zhu, X. Zou, B. Jiang, L. Peng, and Y. Kang, "Power coupling mechanism analysis and improved decoupling control for virtual synchronous generator," *IEEE Trans. Power Electron.*, vol. 36, no. 3, pp. 3028–3041, Mar. 2021.
[23] F. Zhao, X. Wang, and T. Zhu, "Power dynamic decoupling control of grid-forming converter in stiff grid," *IEEE Trans. Power Electron.*, vol. 37, no. 8, pp. 9073–9088, Aug. 2022.
[24] B. Long, S. Zhu, J. Rodriguez, J. M. Guerrero, and K. T. Chong, "Enhancement of power decoupling for virtual synchronous generator: A virtual inductor and virtual capacitor approach," *IEEE Trans. Ind. Electron.*, vol. 70, no. 7, pp. 6830–6843, Jul. 2023.
[25] M. Li et al., "Unified modeling and analysis of dynamic power coupling for grid-forming converters," *IEEE Trans. Power Electron.*, vol. 37, no. 2, pp. 2321-2337, Feb. 2022.
[26] C. K. Sao and P. W. Lehn, "Autonomous load sharing of voltage source converters," *IEEE Trans. Power Del.*, vol. 20, no. 2, pp. 1009–1016, Apr. 2005.
[27] Q. C. Zhong, "Robust droop controller for accurate proportional load sharing among inverters operated in parallel," *IEEE Trans. Ind. Electron.*, vol. 60, no. 4, pp. 1281–1290, Apr. 2013.
[28] H. Tobias, T. Tran, R. David, and M. Antonello, "Power control of Andronov-Hopf oscillator based distributed generation in grid-connected microgrids," in *Proc. Adv. Eng. Res. Appl.*, Springer International Publishing, 2021, pp. 675–687.
[29] T. T. Tran et al., "Enhancing performance of andronov-hopf oscillator-based grid-forming converters in microgrids with non-invasive online impedance estimation," *IEEE Trans. Smart Grid*, vol. 14, no. 6, pp. 4479–4493, Nov. 2023.
[30] R. Sheehan and L. Diana, "Switch-mode power converter compensation made easy," Texas Instrum., Dallas, TX, USA, Tech. Rep. SLUP341, 2016.
[31] A. Karimi and G. Galdos, "Fixed-order $H_\infty$ controller design for non-parametric models by convex optimization," *Automatica*, vol. 46, no. 8, pp. 1388–1394, Aug. 2010.
[32] J. Lofberg, "YALMIP: A toolbox for modeling and optimization in MATLAB," in *Proc. IEEE Int. Symp. Comput. Control Syst. Des.*, 2004, pp. 284–289.
[33] M. ApS, "The MOSEK optimization toolbox for MATLAB manual. Version 9.0," 2019. [Online]. Available: http://docs.mosek.com/9.0/toolbox/index.html.
[34] E. Dall'Anese and A. Simonetto, "Optimal power flow pursuit," *IEEE Trans. Smart Grid*, vol. 9, no. 2, pp. 942–952, Mar. 2018.
[35] Z. Yuan, G. Cavraro, M. K. Singh, and J. Cortés, "Learning provably stable local volt/var controllers for efficient network operation," *IEEE Trans. Power Syst.*, vol. 39, no. 1, pp. 2066–2079, Jan. 2024.

**Mingyue Wang** received the B.S. degree in automation in 2022 from Shandong University, Jinan, China, where he is currently working toward the Ph.D. degree in electrical engineering with the School of Control Science and Engineering.

His current research interests include renewable power generation and stability analysis and improvement.

**Alian Chen** (Member, IEEE) received the B.S degree in electronic application technology and the M.S. degree in power electronics from Shandong University, Jinan, China, in 1998 and 2000, respectively, and the Ph.D. degree in electrical engineering from Zhejiang University, Hangzhou, China, in 2005.

She joined the School of Control Science and Engineering, Shandong University, and was promoted as an Associate Prof essor in 2005, where she has been a Full Professor since 2010. During 2013 2014, she was a Visiting Scholar with the Center for Power Electronics Systems, Virginia Tech, Blacksburg, VA, USA. Her current research interests include multilevel converters, renewable power generation, and microgrids.

**Yaopeng Huang** received the B.S. degree from the Jiangsu University of Science and Technology, Zhenjiang, China, in 2019, and the M.S. degree in control engineering from Hohai University, Nanjing, China, in 2021. He is currently working toward the Ph.D. degree in electrical engineering with the School of Control Science and Engineering, Shandong University, Jinan, China.

His current research interests are multilevel inverters, renewable power generation, and model free predictive control.

**Xianzhe Pang** (Student Member, IEEE) was born in Shandong, China, in 1998. He received the B.S. degree in integrated circuit from the Hefei University of Technology, Hefei, China, in 2020. He is currently working toward the Ph.D. degree in electrical engineering with the School of Control Science and Engineering, Shandong University, Jinan, China.

His current research interests include multilevel inverters, renewable power generation and fault tolerant control.

**Cheng Cheng** (Member, IEEE) received the B.S degree in electronic received the Ph.D. degree in electrical engineering from the Nanjing University of Aeronautics and Astronautics, Nanjing, China, in 2023.

He is currently a Postdoctoral Research Fellow with the School of Control Science and Engineering, Shandong University, Jinan, China. His current research interests include stability analysis and stabilizing control for grid tied converters, energy storage converters and microgrids.

**Tong Liu** (Member, IEEE) received the B.S. degree in electrical engineering from the Harbin University of Science and Technology, Harbin, China, in 2014, the M.S. degree in electrical engineering from the University of Dalian Jiaotong University, Dalian, China, in 2018, and the Ph.D. degree in electrical engineering from Shandong University, Jinan, China, in 2022.

From 2023 to 2025, he was a Postdoctoral with the School of Electrical Engineering, Shandong University. In 2025, he joined the School of Future Technology, Shandong University, where he is currently an Associate Researcher His current research interests include multilevel inverters, renewable power generation, power instrument and predictive control.